JOURNAL OF AIRCRAFT
Vol. 40, No. 5, September–October 2003

Navier–Stokes Simulations for Transport Aircraft Wing/Body High-Lift Configurations

HaiXin Chen* and Song Fu†
Tsinghua University, 100084 Beijing, People's Republic of China
and
FengWei Li‡
Northwestern Polytechnical University, 710072 Xi'an, People's Republic of China

A novel multiblock grid approach, the multilayer window embedment technique, is introduced. With this approach, the Navier–Stokes equations are solved numerically for realistic transport wing/body high-lift configurations. Results for two configurations are presented and compared with experimental data.

Introduction

TO achieve sufficient lift, a modern transport aircraft usually deploys slats and flaps to form a high-lift configuration during landing or taking off. In the whole process of the aerodynamics design of a transport aircraft, the design of the high-lift system is often a pacing item. Computational fluid dynamics (CFD) is playing an ever more active role in the aircraft's aerodynamics design. To reduce the wind-tunnel test costs and the design cycle time, significant efforts are now underway in the development of CFD techniques for high-lift system design.

Much progress has been achieved in the CFD analysis of two-dimensional high-lift systems.[1] Comparatively few studies on three-dimensional high-lift systems have been reported.[2–4] This is especially the case for the numerical simulation of complete aircraft high-lift configurations.[5–8] Although two-dimensional CFD analysis can provide benefits to the high-lift system design to some extent, high-lift flows are inherently three dimensional.[6]

The great difficulties of CFD simulation of a realistic aircraft with deployed high-lift system lie in both the aircraft's complex geometry and the relevant extremely complex flow features. The geometry of the three-dimensional high-lift configuration is characterized by multi-elements and the existence of geometry discontinuities at places such as flap ends both cause severe problems to structured grid generation approach. The high-lift flow is dominated by various flow phenomena, such as flow separation, complex vortices, wakes, and wake/boundary interaction. Although the working speed range is limited to low Mach number, due to the flow acceleration, shock wave and shock–boundary interactions may still occur inside the narrow gaps between slat and main wing. In addition to the requirement of a powerful grid generator, the complexity of the flow phenomena and the wide range of their characteristic scales demand a high-resolution, high-accuracy, and robust numerical solver with adequate choices of turbulence models.

To provide the high-lift system designers with an analysis tool of acceptable accuracy and efficiency, we recently developed the CFD code called HLNSWE. The background of the present research is the development of the Chinese airliner ARJ-21. To gain deep insights into the mechanism of high-lift flow and to provide calibration data for CFD research, a wind-tunnel model of a transport wing/body combination with high-lift devices was built and tested. The HLNSWE code was calibrated with the test data, and HLNSWE then played a role as the analysis tool in the preliminary aerodynamics design of ARJ-21. After several rounds of design iteration, a configuration was obtained with most of the design targets reached. wind-tunnel tests were again performed with the optimized configuration to verify the design effects, as well as the accuracy of CFD analysis.

The HLNSWE consists of a grid generator and a flow solver. The core methodology is a novel multiblock structured grid technique, the so-called multilayer window embedment (MLWE) technique, which solves the problems that accompany multi-element and geometry discontinuities very well. When a flexible arrangement of grid density and topology in different grid blocks is allowed, the multiscale nature of the high-lift flow can be captured with a comparatively small number of grids. This paper introduces the ideas and the methodologies employed in HLNSWE. The capability and performance of HLNSWE for high-lift computation are assessed on the numerical simulations of two wind-tunnel models. Computed results and its comparisons with the experimental data are presented and analyzed.

Numerical Methods

Flow Solver

The cell-centered finite volume methods (CCFVM)[9] are employed to solve the Reynolds-averaged compressible Navier–Stokes equations. Steady-state results are obtained through an explicit four-stage Runge–Kutta time stepping. The Jameson-type blended second- and fourth-order artificial viscosity is added to the essentially central differencing spatial scheme for the suppression of the spurious numerical oscillation. According to Radepiel and Rossow,[10] the scaling factors are reformulated to adapt to the grid cells' aspect ratio. Some modifications of convergence acceleration techniques are also introduced to improve the robustness, efficiency, and accuracy of the method.

Turbulence Modeling

The turbulence model adopted in the present version is the Baldwin–Lomax model. Although it is commonly thought of as not suitable for high-lift flow simulation, this simple algebraic model demonstrates fairly good convergence and allows the use of comparatively coarse grids. The k–ω shear-stress transport (SST) and spalart-allmaras (S–A) models are now being incorporated into the HLNSWE code to improve its capability of accurately predicting flow separation, which is important to high-lift flow. However, the present emphasis is not focused on turbulence modeling.

Received 29 April 2003; revision received 30 April 2003; accepted for publication 9 June 2003; presented as Paper 2003-4077 at the 21st AIAA Applied Aerodynamics Conference, Hilton at Walt Disney World, Orlando, FL, 23 June 2003.

*Lecturer, Department of Engineering Mechanics.

†Professor, Department of Engineering Mechanics. Member AIAA.

‡Professor, Department of Aircraft Engineering.

Patched Block Interface

The multiblock grid technique in HLNSWE is based on the patch grid technique. Three patch patterns are allowed for interfacing different blocks.

Point-to-Point Patch

The grid lines are designed to be continuous with one-to-one grid matching at the block interfaces. For CCFVM, point-to-point patch demands the least coding work on the information exchange between grid blocks and theoretically has no risk of accuracy deterioration on the grid interfaces. However, the requirement for one-to-one matching will decrease the flexibility in arranging grid density and topology in the grid blocks. The grid clustering in one block will often have to be extended to adjacent blocks, where no clustering is needed.

Although extremely complex, point-to-point patch was successfully applied by Takallu and Laflin[2] to the computation of partial-span flap wing. As many as 21 blocks are used in that effort.

Surface Patch

When geometry discontinuity exists or grid topology changes across the block interface, the one-to-one matching of grid lines is difficult to achieve. The technique of overlap area-weighted reconstruction (OAWR) of conservative flow parameters is used for field information exchange to allow point discontinuous block interfacing.

OAWR was developed by Kathong et al.[11] and used by Chin[12] in his interactive boundary-layer/Euler computation about wing/body combination with deflected ailerons. For simplicity, the idea can be explained as the two-dimensional map in Fig. 1. Grid blocks 1 and 2 patched on the interface are drawn by dashed and solid lines and labeled by indices (j, k) and (m, n), respectively. When the phantom grid technique is used at the interface, a dummy grid cell $(j, k+1)$ can be created for cell (j, k) in block 1. According to the CCFVM's formulation, the flux on cell surface $(j, k+\frac{1}{2})$ can be written as

$$\mathrm{Flux}_{\left(j,k+\frac{1}{2}\right)} = \frac{(\boldsymbol{h}_{j,k}+\boldsymbol{h}_{j,k+1})}{2}A_{j,k+\frac{1}{2}}$$

$$= \frac{(\boldsymbol{h}_{j,k}+\boldsymbol{h}_{j,k+1,m+1,n})}{2}A_{j,k,m+1,n} + \frac{(\boldsymbol{h}_{j,k}+\boldsymbol{h}_{j,k+1,m,n})}{2}A_{j,k,m,n}$$

$$= \frac{(\boldsymbol{h}_{j,k}+\boldsymbol{h}_{m+1,n})}{2}A_{j,k,m+1,n} + \frac{(\boldsymbol{h}_{j,k}+\boldsymbol{h}_{m,n})}{2}A_{j,k,m,n}$$

where $\boldsymbol{h}$ is the conservative parameter. $\boldsymbol{A}_{j,k,m,n}$ is the portion of the area of cell (j, k) overlap with cell m, n. With N the number of cells in block 2 that overlap with cell (j, k), $\boldsymbol{h}$ in the dummy cell $(j, k+1)$ can be expressed in a more general form[12]:

$$\boldsymbol{h}_{j,k+1} = \sum_{l=1}^{N} \boldsymbol{h}_{(m,n)_l} \frac{A_{j,k,(m,n)_l}}{A_{j,k+\frac{1}{2}}} \tag{1}$$

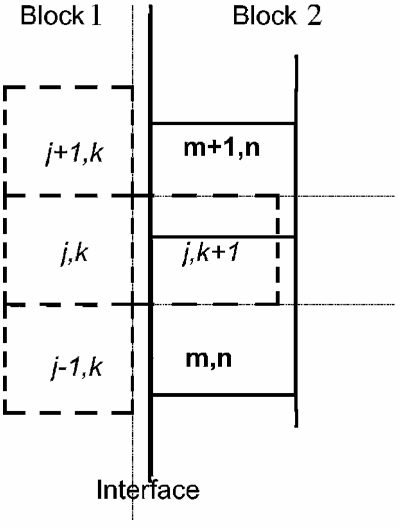

Fig. 1 Two-dimensional map for mismatch grid interface.

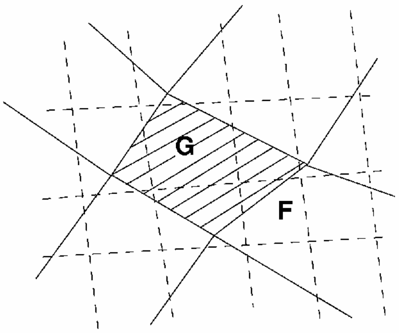

Fig. 2 Plane view of surface patch grid interface.

Thus, the flow parameters in the fictitious grid cells, which are needed by the interface flux computation of the block 1 cells, are reconstructed with the parameters in block 2's boundary cells according to their overlap area. From the deduction procedure, it is easy to understand that, when incorporated into CCFVM, this technique guarantees the global flux conservation on the block interfaces.

In three-dimensional cases, as shown in Fig. 2, the grid lines of both block 1 (solid lines) and block 2 (dashed lines) intersect each other on the interface. The line segments buildup the envelopes of the overlap zones. The shape of the zones may be triangle, quadrilateral, pentagon, and so on. The overlap relation between two blocks' boundary cells may be so complex that we have to use the Ramshaw algorithm[13] to determine N and $A_{j,k,(m,n)_l}$ in Eq. (1). The Ramshaw algorithm is based on the area equation of general n-sided polygon P:

$$A_P = \frac{1}{2}\sum_{s=1}^{n} \varepsilon_s^P \left[x_1^s y_2^s - x_2^s y_1^s\right] \tag{2}$$

where $S1$ and $S2$, which are holding the coordinates (x_1^s, y_1^s) and (x_2^s, y_2^s), respectively, are the two endpoints of the sth side of P and ε_s^P is either $+1$ or -1, depending on whether P lies on the left or right side when $S1$ faces $S2$, respectively.

Equation (2) breaks the area down into contributions from all of the n line segments and sums them. Following this idea, if G is a cell (shaded) of block 1, its fictitious cell's conservative parameter h^G can also be computed by collecting the contributions from all of the line segments within G or on its boundaries. The formulations can be expressed as follows.[13]

When s is a segment of block 2's grid line,

$$\Delta h_s^G = (1/2A_G)(h_L - h_R)\left(x_1^s y_2^s - x_2^s y_1^s\right) \tag{3}$$

where h_L and h_R are the h values in the block 2 cell left and right to s, respectively.

When s is a segment of block 1's grid line,

$$\Delta h_s^G = \left(\varepsilon_s^G/2S_G\right)h_F\left(x_1^s y_2^s - x_2^s y_1^s\right) \tag{4}$$

where F is the grid cell of block 2 in which s lies.

Sweep all of the grid lines of both blocks 1 and 2 one by one, compute each segment's contribution with Eqs. (3) or (4), and add it to the h value of the block 1 cell where the segments lies. With the simple and uniform procedure, OAWR can be performed with little increase in the total computation time.

Some special treatment must be performed when the interface encounters geometry discontinuity. As shown in Fig. 3, the inboard and outboard flap have different deflection angles. In this case, the blocked area occupied by the flap end in block 2 is divided into dummy cells. When cell L, R, or F in Eqs. (3) and (4) is a dummy grid, the respective h_L, h_R, or h_F will be set equal to the G's fictitious cell value for no-slip boundary conditions.

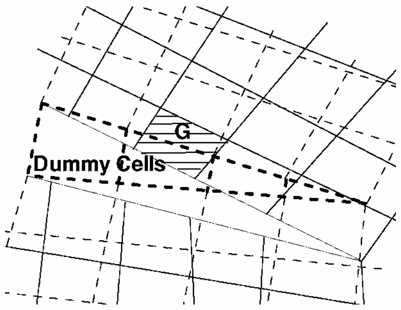

Fig. 3 Wall boundary treatment for surface patch.

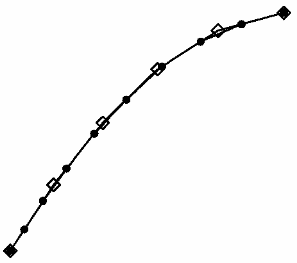

Fig. 4 Two patched grid lines before paring: ●, line 1, original and ◇, line 2, original.

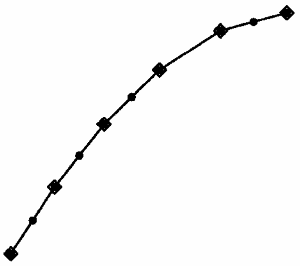

Fig. 5 Two patched grid lines after paring: ●, line 1, processed and ◇, line 2, processed.

The surface patch technique reduces the troublesome work of dealing with the mutual restrictions of grid topology and density between grid blocks in grid generation. Hence, appropriate grid density and topology can be arranged principally according to the flow and geometry requirement.

Quasi-Point-to-Point Patch

As is well known, two grid surfaces discretized from the same curved surface will hardly be identical if the arrangements of grid points are different. Therefore, to maintain strictly the conservation and accuracy, the surface patch technique requires the interfaces to be planar. This rigorous restriction limits the application of the surface patch.

When both of the patched grids are generated by stacking two-dimensional grids, the study of the patching relation between the three-dimensional grids can be focused on that of their spanwise profile's edge lines. Figure 4 shows two grid lines. The numbers and clustering of the nodes on them are different. Obvious mismatch can be found.

Let A and B be two nodes on lines 1 and 2, respectively. Sweep all of the nodes on the two lines. If the nearest node on line 2 to A is B, and the nearest node on line 1 to B is A, then move the two nodes to a same point, for example, the midpoint of them, which is labeled as a paired node. Repeat the procedure until between two adjacent pair nodes there are only unpaired nodes on either line. Move the unpaired nodes on to the joint line of the pair nodes by linear interpolation. Such a process is called pairing. Figure 5 shows the two lines after the pairing process. All of the deviations between them are eliminated. The pared nodes are certainly one-to-one matching. This is why the quasi-point-to-point patch is so named.

With the quasi point-to-point patch, OAWR can be performed on spanwise stretching bended interfaces. Because of the paring process, the overlap relation can be determined with great ease.

Window Embedment Strategy

Grid

A novel multiblock structured grid generation approach, window embedment (WE) technique is employed. To explain the idea of the method, the procedure of the grid generation about a two-dimensional multi-element airfoil is used as an example.

A C-type grid is first generated about the baseline of the airfoil without consideration about the cut for flap, as shown in Fig. 6. A window of interest is then assigned on the C-grid by selecting a range of grid index in both the I and J directions. The window must be large enough to hold the flap. As shown in Fig. 7, an H-type grid about the flap is generated inside the window with its outer boundaries coinciding with the window's envelope lines. The cove at the main airfoil is now mimicked as a section of the upper boundary of the flap grid window.

When applied to realistic configurations, this window concept is extended to a three-dimensional form that is usually in a cube shape with curved surfaces. For the same case of the partial-span flap wing in Refs. 2 and 3, a three-dimensional window is assigned for the flap in the C–H grid about the wing. Inside the window, two blocks of H–H grid is embedded to describe the flap. Altogether, only three grid blocks are required for numerical computation with the present approach (Fig. 8).

Computation

With the three patch methods, flowfield information is exchanged, during the numerical computation, in a conserved manner between baseline and embedded grids at the window envelope surfaces represented by the bold solid line in Fig. 9. Although the baseline grid cells within the window do not contribute to the flowfield computation, they are kept in the iteration to maintain the integrity of the baseline grid's indices. The cells adjacent to the window envelope, such as those marked by O (Fig. 9), may play the role of fictitious cells for the baseline grid's block interface boundary treatment by storing the conservation parameters reconstructed from the

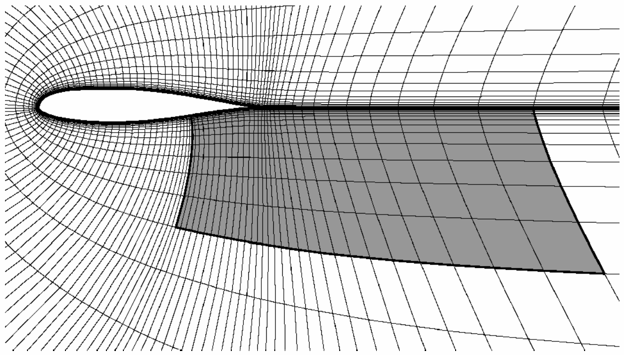

Fig. 6 Window on wing grid.

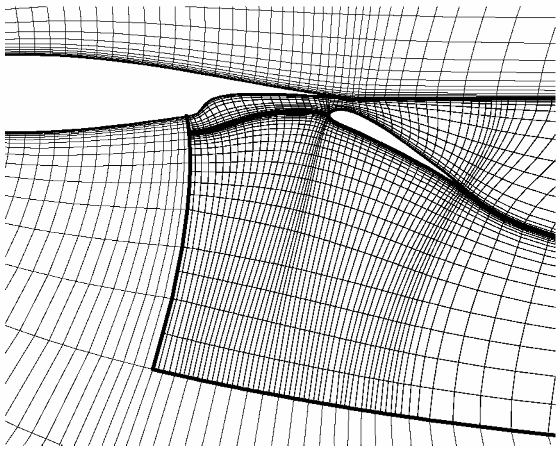

Fig. 7 Flap grid in the window.

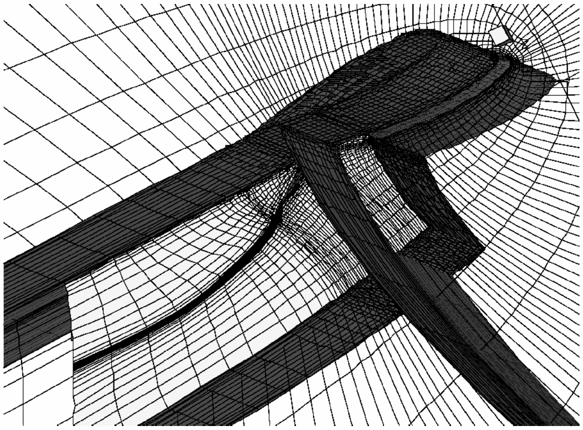

Fig. 8 Three-dimensional WE grids for partial span flap wing.

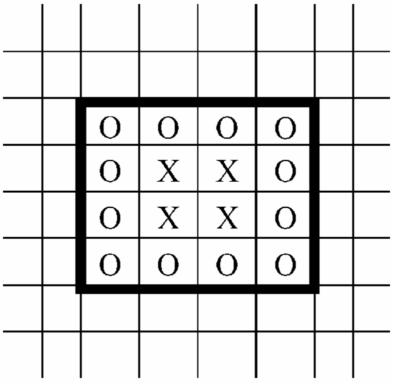

Fig. 9 Treatment of cells inside window.

embedded grids. The correct flow information of the field region enclosed by the window is provided by the embedded grids. The erroneous information in the X cells does not enter the flow computation. The computation cost on the X cells is usually negligible because of their comparatively small number.

The WE technique is somewhat like a combination of the chimera grid technique and the patch grid technique. On the one hand, WE takes the advantages of the chimera technique's embedding idea, which makes it able to decompose a complex configuration into clean parts and then generate grids for them separately. On the other hand, unlike the Chimera grid technique, the grid blocks are clearly separated by interface surfaces, the window boundaries. No grid overlap occurs in WE, and therefore, no spatial interpolation in flow quantities of different grid meshes, which is often the cause for nonconservation in the computation, is required.

With the WE strategy, HLNSWE is especially good at handling complex configurations that can be decomposed into a main body and accessorial parts. Fewer grid blocks are required for the computation than those for the patch grid technique because the baseline grids are kept as a whole. Conflicts sometimes exist in grid density arrangement for these kinds of configurations. The accessorial parts are usually relatively small in size and often need finer grids to reveal the flow details. However, using grid of the same density to the main body is usually neither necessary nor affordable. The present method can truncate the grid clustering at the block interfaces. Hence grid waste is avoided.

The automation of grid generation is critical for a CFD code to be practically used in engineering design. When generating multiblock grids, the defining of the block boundaries usually demands a great deal of manual manipulation. In WE, this time-consuming labor can be avoided. The block boundaries of embedded grids are constructed along the envelopes of the windows, the existent baseline grid surfaces. No more geometric modeling is needed. In this sense, the process of WE grid generation can be automated with greater ease.

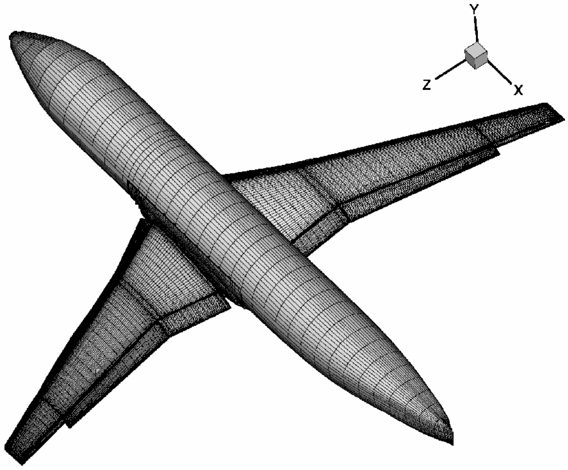

Fig. 10 Model 1 configuration and surface grid.

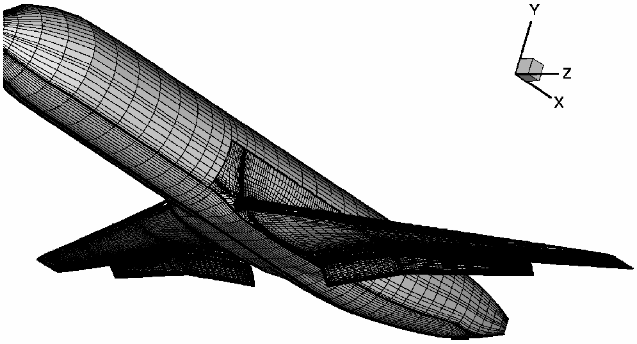

Fig. 11 Model 2 configuration and surface grid.

High-Lift Transport Configurations

Flowfields about two wind-tunnel models of a civil transport high-lift configuration have been experimentally studied in the low-speed wind tunnel of Nanjing University of Aeronautics and Astronautics and are numerically simulated with HLNSWE.

Model 1 is the wing/body combination model that originated from the now-abandoned Chinese AE-100 airliner (Fig. 10). The AE-100 was designed to be a 100-seat commercial aircraft with low wings mounted with twin jets. For purpose of the high lift, the supercritical wing has been reshaped to host deployable slats and single-slotted flaps. The model has a half-span of 1.75 m. The inboard/outboard segmentation of the slat and flap is at about 33% half-span. The slats cover the whole span, whereas the outboard flap ends at 80% span. The deflection angle of slat and flap are set to 25/40 deg for the landing configuration and 17/20 deg for the takeoff configuration.

Model 2 is a preliminary design of the Chinese airliner ARJ-21 (Fig. 11) currently under development. The high-lift system is of greater complexity because the flaps are double-slotted (vane/flap) ones. The slat and flap are split spanwise at 38% half-span. The outboard slat and flap ends at 94 and 75% half-span, respectively.

The size of the wind-tunnel's test section is 3×2.5 m. In both models' tests, the freestream Mach number is 0.2, and the Reynolds number based on the mean aerodynamics chord is 2×10^6.

Grid Generations

The grids in each block are generated with elliptical methods developed by Thompson et al.[14] Hilgenstoke's method[15] is applied to adjust the source terms to control the spacing and orthogonality of the grid lines near the boundaries. When WE is applied to the three-dimensional configurations of wing/body combination with slats and flaps, an O–H-type baseline grid is first generated for the clean fuselage. According to the position and size of the wing, a window is assigned in the baseline grid (Fig. 12). A C–H grid system wrapping around the wing is then embedded in the window.

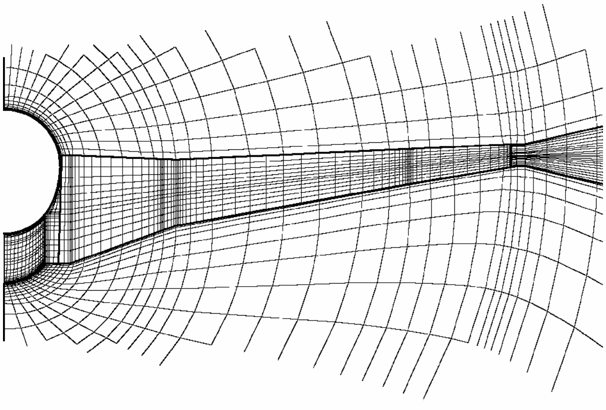

Fig. 12 Wing grid embedded in fuselage grid window (axial profile).

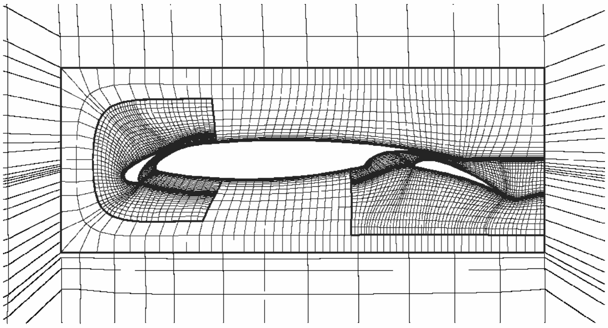

Fig. 13 Spanwise profile of fuselage/wing/flap/slat grid of model 1.

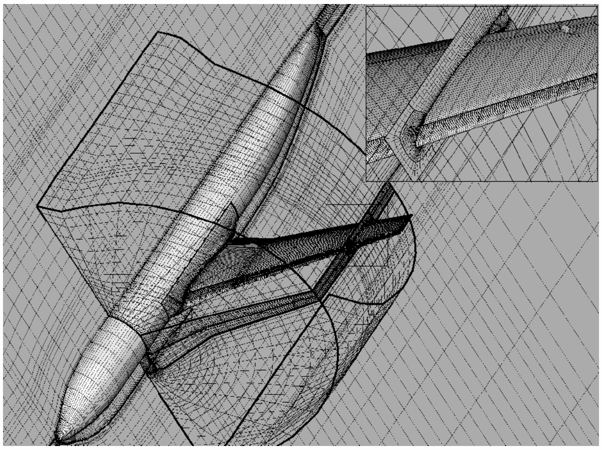

Fig. 14 Model 1 spatial grid.

With the same strategy, four windows are assigned on the wing grid, two for slats and two for flaps. In each window, two blocks of H–H grid systems are generated for the flap or slat, one at the upper side and the other at the lower side. To these blocks, the wing grids succeed those of the fuselage as the baseline grids. In this way, the WE can be recursively applied and, therefore, MLWE is achieved. Figure 13 shows the three-layer embedment in a spanwise profile.

In the present computation a total of 8.6×10^5 grid points in 15 blocks are employed to simulate model 1. Figure 14 shows the spatial topology and embedment relationship of the grids with global and closeup views of some characteristic grid surfaces. It is easy to see that the grid lines between layers in Figs. 12 and 13 are quasi-point-to-point patched. Grid density increases gradually from outer layer to inner layer to ensure appropriate grid resolution for regions with different characteristic flow scales.

Figure 15 shows one case of the treatment for geometry discontinuity in model 1. The outboard flap ends at 80% span. Therefore, the surface patch technique is adopted here for interfacing between the flap grid (solid lines) and the baseline wing grid (dashed lines) outside the flap window.

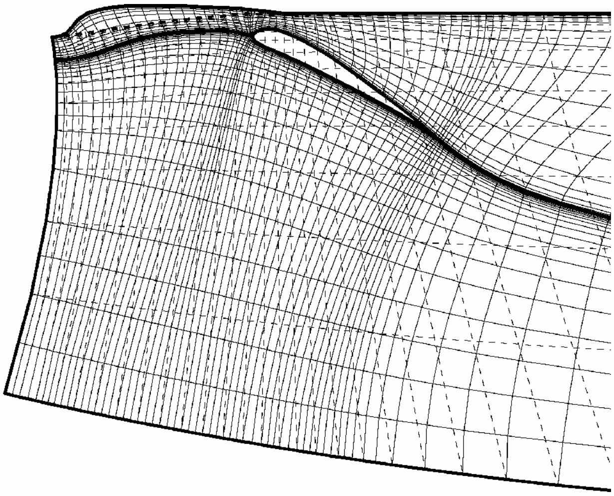

Fig. 15 Surface patch grid interface at outboard flap end.

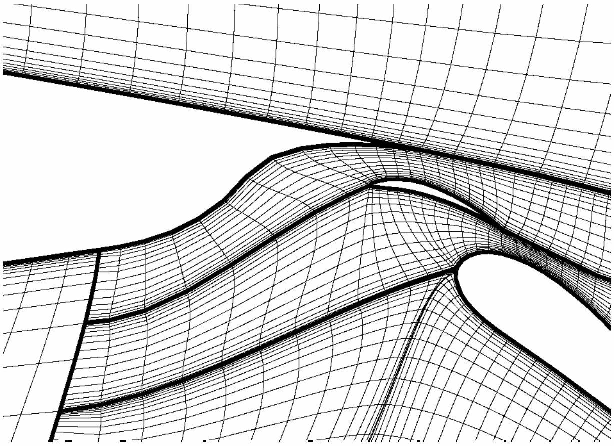

Fig. 16 Span-wise profile of wing/slat/vane/flap grid of model 2.

For model-2, one H–H grid block is added in each of the flap windows to simulate the vane. Figure 16 shows the difference with Fig. 13. Both computation models strictly resemble the respective wind-tunnel models. The wind-tunnel wall is not considered in the grid generation because the experimental results claimed to have wall interference corrected.

Numerical Results

Three configurations, corresponding to cruise, landing, and takeoff situations, are computed for the two models. In the cruise case, the flaps and slats are stowed. In the present MLWE grid generation, the wing grid system is generated for the cruise condition (as described in the "Window Embedment Strategy," "Grid" subsection). The shape of the main wing when flaps and slats are deployed is corrected to its carved status by the embedded grids. Thus, when the flap and slat windows switch off, the computation will be right back for the cruise configuration. Also with great ease, from the landing configuration to the takeoff configuration, nothing but the flap- and slat-window grids are substituted.

Lift coefficients vs AOA are plotted in Figs. 17a–17c with comparison to experimental data for all three configurations of model 1. The lift curves compare fairly well with test data in the linear range. The angle of maximum lift in the computation results for the cruise configuration is behind by about 3 deg. The reason is attributed to the occurrence of flow separation in the cruise case because the wing without slat and flap is more likely to cause flow separation at high AOAs. It is believed that the present turbulence model can not appropriately resolve the flow separation accurately.

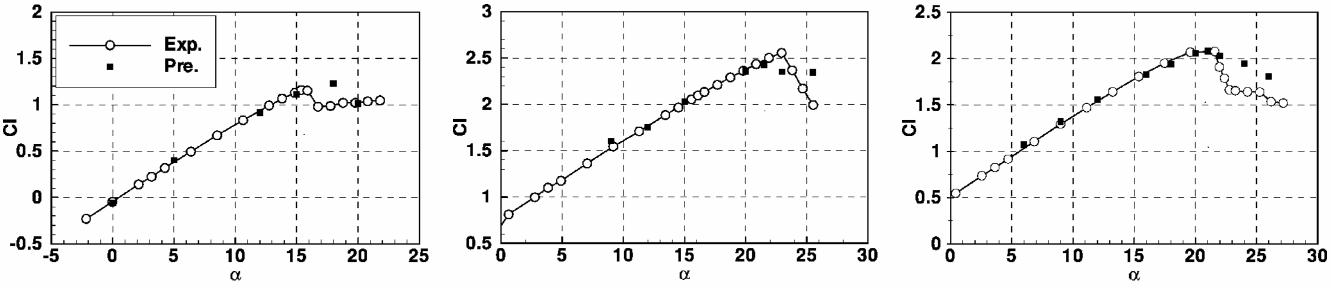

a) Cruise

b) Landing

c) Takeoff

Fig. 17 Lift curves of model 1.

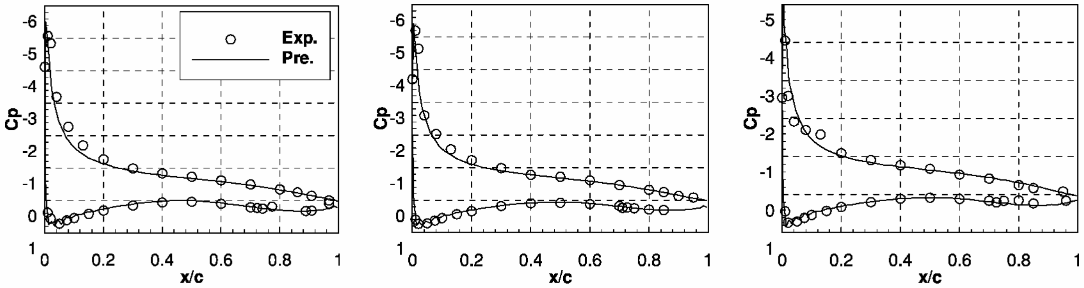

a) 21% span

b) 40% span

c) 72% span

Fig. 18 Pressure coefficient of model 1's clean configuration, $\alpha = 9$ deg.

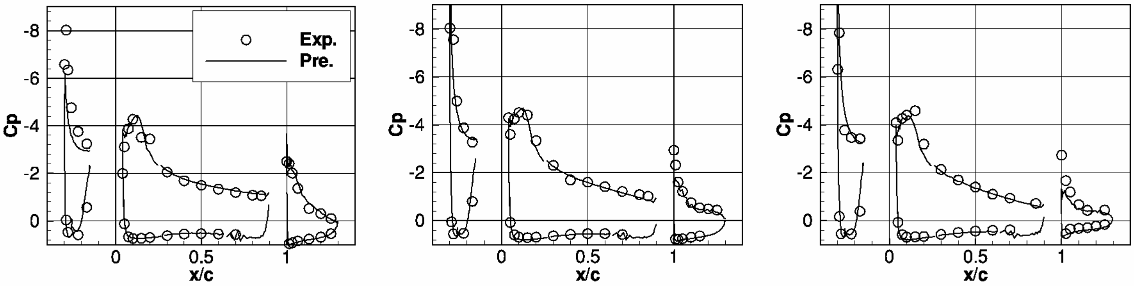

a) 21% span

b) 40% span

c) 72% span

Fig. 19 Pressure coefficients of Model 1's landing configuration, $\alpha = 17$ deg.

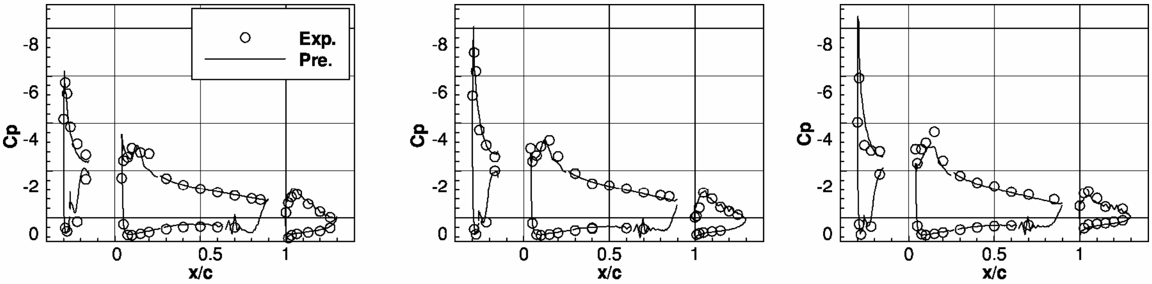

a) 21% span

b) 40% span

c) 72% span

Fig. 20 Pressure coefficient of Model 1's takeoff configuration, $\alpha = 13$ deg.

Similar problems can be found in the results of the landing and takeoff cases. For the landing configuration, the predicted angle of maximum lift is earlier than the experimental data. However, for the takeoff configuration, the angle seems to be well predicted. The steep drops in the lift after the maximum AOA are not simulated well for all three configurations. All of these disagreements demonstrate the inadequacy of the present turbulence model to massive separation at high AOA.

For the pressure distribution at the spanwise stations for the cruise configuration's computational results, the agreements with experimental data are good (Fig. 18). A slight overprediction of the suction peak at leading edge can be seen. Besides the accuracy of the present

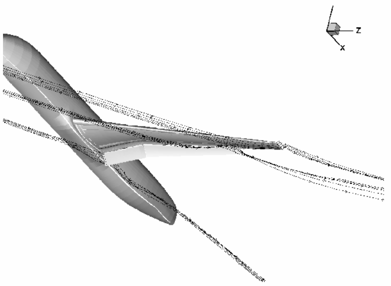

Fig. 21 Spatial streamlines for model 1, $\alpha = 15$ deg.

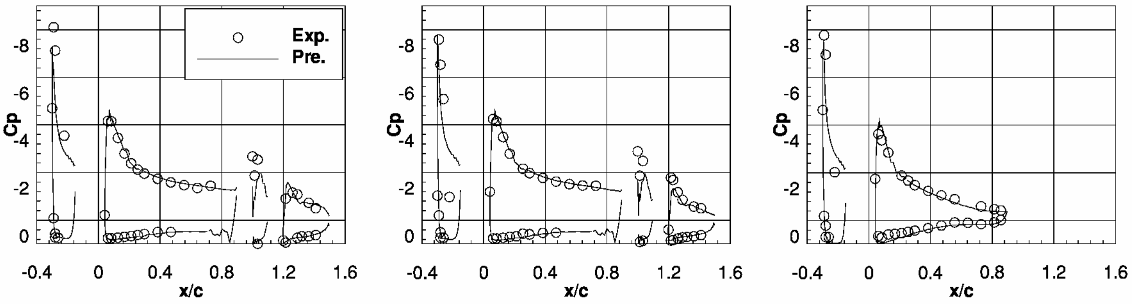

a) 21% span b) 40% span c) 72% span

Fig. 22 Pressure coefficient of model 2's landing configuration, $\alpha = 16$ deg.

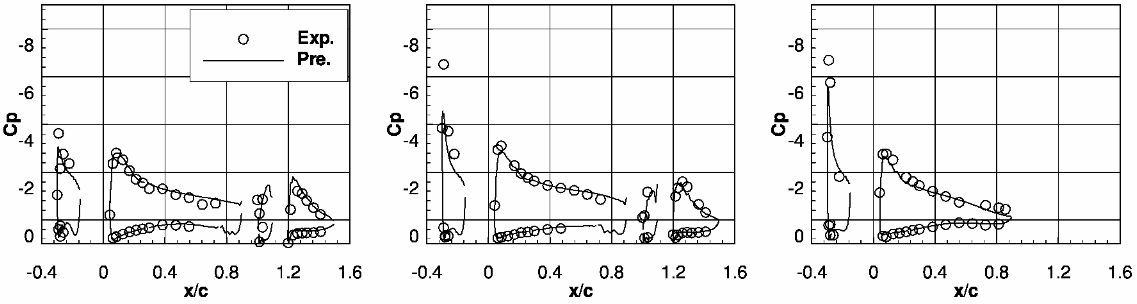

a) 21% span b) 40% span c) 72% span

Fig. 23 Pressure coefficient of model 2's takeoff configuration, $\alpha = 12$ deg.

method, an insufficient number of pressure transducers may also be responsible.

The results for the landing configuration are also satisfying. At the AOA of 17 deg, the flow separation spread from outboard to inboard on the upper surface of flap, as shown by the position of the upward bend on the pressure coefficient curves of both numerical and experimental results (Fig. 19). The H–H topology of flap grids demonstrates its disadvantage in leading-edge flow simulation. Nonphysical leading-edge separation and the consequent numerical instability will occur at high AOA. This should be responsible for the underpredicted suction peak of the flaps. Such a problem is not as serious in the results of the takeoff configuration in Fig. 20 because the local AOA of the flap is lowered by the smaller deflection angle.

In Fig. 21, the vortexes rolling up from the gap between the fuselage and the edge of inboard flap, from the edge of the outer flap, and from wing tip are seen clearly, demonstrating the ability of HLNSWE in capturing the flow details. At all of these edges, the surface patch technique is applied. The streamlines cross the grid interfaces smoothly. The feasibility of OAWR in dealing with geometry discontinuity is verified.

The results of pressure distribution are also presented for model 2's two high-lift configurations (Figs. 22 and 23). The computational results are also in good agreement with experimental data. The agreement of the results at the vanes is not as satisfying as at other parts. This is because of the small size and thickness of the vane, which requires both high grid resolution in the computation and high-pressure transducer density in the experiment.

Although it is inherently easy to be modified to a parallel version, the HLNSWE is currently run in a scalar manner. On a PentiumIII 733-MHz class personal computer with 384MB main memory, it takes about 20 h to run 4000 iterations for model 1. At a medium angle of attack (AOA), this number of iteration is usually sufficient to have the residual decreased by 3 orders and the variation of lift coefficient in the last 100 iterations reduces to under 0.5%. As a reference frame, it took the author about two work months to set up the geometry and generate grids about the landing configurations of Model-1. However, with this basis, the grid generation about each of the other configurations was accomplished within a single week, despite the geometry difference between model-2 and model-1.

Conclusions

The HLNSWE code is used to simulate numerically the flowfield about high-lift configurations of transport aircraft. Results of cruise, takeoff, and landing geometries are presented for two design models with realistic complexity. The computed results in the linear range are in good agreement with experimental data. The satisfying computational results, which have been utilized in the aircraft design process, have validated the present method for application to complex three-dimensional high-lift problems.

The MLWE technique greatly reduces the difficulties of grid generation for complex geometries and dramatically decreases the numbers of both grid block and total grid point while ensuring the necessary grid resolution at key flow regions. The surface patch technique makes the simulation of geometry discontinuity very simple. The OWAR technique guarantees the global conservation at the mismatch interfaces. However, detailed simulation of viscous phenomena at places such as the flap and slat edges[3] needs more carefully design of grid embedment.

At the AOAs above maximum lift, much work on turbulence modeling has to be done to improve the accuracy and reliability of the present computation results. Although k–ω and S–A models are commonly known as the best choices in high-lift research, their performance in predicting the flowfield near stall is still not adequately satisfactory.[6,8]

Limited by the computer resources, the present computations employ a relatively very small number of grid points, significantly less than the other reported similar work by an order or two. In addition to the errors in test data and inadequate turbulence modeling, the poor grid density is another primary factor that should be responsible for the disagreement between computational results and test data. For the improvement of the HLNSWE code's capability, parallelization is believed to be a good measure, and the code is being implemented thusly.

References

[1] Rogers, S. E., "Progress in High-Lift Aerodynamics Calculations," *Journal of Aircraft*, Vol. 31, No. 6, 1994, pp. 1244–1251.

[2] Takallu, M. A., and Laflin, K. R., "Reynolds-Averaged Navier–Stokes Simulations of Two Partial-Span Flap Wing Experiment," AIAA Paper 98-0701, Jan. 1998.

[3] Mathias, D. L., Roth, K. R., Ross, J. C., Rogers, S. E., and Cummings, R. M., “Navier–Stokes Analysis of the Flow About a Flap Edge,” AIAA Paper 95-0185, Jan. 1995.

[4] Baker, M. D., Mathias, D. L., Roth, K. R., and Cummings, R. M., “Numerical Investigation of Slat and Compressibility Effects for a High-Lift Wing,” AIAA Paper 99-0538, Jan. 1999.

[5] Cao, H. V., Su, T. Y., and Rogers, S. E., “Navier–Stokes Analysis of a 747 High Lift Configuration,” AIAA Paper 98-2623, June 1998.

[6] Slotnick, J. P., An, M. Y., Mysko, S. J., Yeh, D. T., Rogers, S. E., Roth, K., Baker, M. D., and Nash, S. M., “Navier–Stokes Analysis of a High Wing Transport High-Lift Configuration with Externally Blown Flaps,” AIAA Paper 2000-4219, Aug. 2000.

[7] Rogers, S. E., Roth, K., Cao, H. V., Slotnick, J. P., Whitlock, M. E., Nash, S. M., and Baker, M. D., “Computation of Viscous Flow For a Boeing 777 Aircraft in Landing Configuration,” AIAA Paper 2000-4221, Aug. 2000.

[8] Rudnik, R., Melber, S., Ronzheimer, A., and Brodersen, O., “Three-Dimensional Navier–Stokes Simulations for Transport Aircraft High-Lift Configurations,” *Journal of Aircraft*, Vol. 38, No. 5, 2001, pp. 895–903.

[9] Jameson, A., Schmidt, W., and Turkel, E., “Numerical Solution of the Euler Equations by Finite Volume Methods Using Runge–Kutta Time-Stepping Schemes,” AIAA Paper 81-1259, June 1981.

[10] Radepiel, R., Rossow, C.-C., and Swanson, R. C., “Efficient Cell-Vertex Multigrid Scheme for Three-Dimensional Navier–Stokes Equations,” *AIAA Journal*, Vol. 28, No. 8, 1990, pp. 1464–1472.

[11] Kathong, M., Smith, R. E., and Tiwari, S. N., “A Conservative Approach for Flow Field Calculation on Multiple Grids,” AIAA Paper 88-0224, Jan. 1988.

[12] Chin, V. D., “Transonic Calculation for Wings with Deflected Control Surfaces,” AIAA Paper 92-2617, June 1992.

[13] Ramshaw, J. D., “Conservative Rezoning Algorithm for Generalized Two-dimensional Meshes,” *Journal of Computational Physics*, Vol. 59, 1985, pp. 193–199.

[14] Thompson, J. F., Thames, F. C., and Mastin, C. W., “Automatic Numerical Generation of Body-Fitted Curvilinear Coordinates for a Field Containing any Number of Arbitrary Two-Dimensional Bodies,” *Journal of Computational Physics*, Vol. 15, No. 3, 1974, pp. 299–319.

[15] Hilgenstock, A., “A Fast Method for the Elliptic Generation of Three Dimensional Grids With Full Boundary Control,” *Numerical Grid Generation In Computational Fluid Mechanics ’88*, Pineridge, Swansea, Wales, U.K., 1988, pp. 137–146.